Cellulose nanocrystals' assembly under ionic strength variation: from high orientation ordering to random orientation

*Daria Bukharina, Minkyu Kim, Moon Jong Han, Vladimir V. Tsukruk**

School of Materials Science and Engineering, Georgia Institute of Technology, Atlanta, GA 30332, USA

Abstract

We discuss the effect of the ionic strength and effective charge density on the final structural organization of cellulose nanocrystal (CNCs) after drying suspensions with different ionic strengths in terms of quantitative characteristics of orientation order, rarely considered to date. We observed that increasing ionic strength in initial suspension results in continuous shrinking in helical pitch length that shifts the photonic bandgap to a far UV-region from visible range (from 400 nm to 250 nm) because of the increasing in helical twisting power from 4 to 6 μm^{-1} and doubling twisting angle between neighboring monolayers from 5.5° to 9°. As our estimation of the Coulombic interactions demonstrates, the reduction of the Debye charge screening length below critical value of 3 nm results in loss of the long-range helicoidal order and in transition to disordered morphology with random packing of nanocrystals. Subsequently, very high orientation ordering with 2D orientation factor, S, within 0.8-0.9, close to theoretical limit of 1, gradually decreased to very low S = 0.1-0.2, a characteristic of random organization at high ionic strength. We suggest that loss of the chiral ordering is a result of the reduction of repulsive forces promoting direct physical contact with reduced contact area during Brownian motion combined with increased repulsive Coulombic interactions of nanocrystals at non-parallel local packing. Notably, electrolyte addition enhances chiral interactions to the point when the helical twisting power is too large and the resulting nanocrystal bundles can no longer compactly pack without creating unfavorably large free volume. We propose that Debye charge screening length in suspensions can be used as universal parameter for CNCs under different conditions and can be used to assess expected ordering characteristics in the solid films.

***Keywords**: cellulose nanocrystals organization, colloidal interactions, chirality control, chiral nematic assembly, orientation order parameters*

* *Corresponding author:* E-mail: vladimir@mse.gatech.edu

Introduction

Biophotonic materials are capable of *chiroptical sensing, bioselective sensing, directed emission, and thermal and microwave vision*. Chiral optical materials and special classes of optical metamaterials exhibit strong discrimination of circular polarization of light due to chiral asymmetry, thanks to their unique chemical structures and organization.[1,2,3,4] Bio-derived materials have advances to meet requirements for the next generation soft photonic materials because they are lightweight, easily processable, and synergistically combine strength and functionality to yield enhanced functional utilities and exceptional mechanical and optical properties not seen in inorganic materials.[5,6] Polysaccharide biopolymers (cellulose and chitin, specifically) are the most abundant polymers and therefore, attracted researchers' interest for wide range of applications including photonics applications in molecular sensing, super-resolution imaging, data storage and optical encryption.[7,8,9,10,11]

Cellulose nanocrystals, obtained by acid hydrolysis of cellulose, are one-dimensional stiff needles with high aspect ratio (typical width 5-20 nm vs lengths in sub/micrometers range).[12,13,14] Due to inherited surface charge, CNCs demonstrate great dispersion stability, which in combination with their abovementioned high aspect ratio, allows them to self-assemble into a left-handed chiral nematic liquid crystal (LC) phase upon critical concentration. Onsager predicted that the solution of rigid rods will undergo a phase transition into an orientationally-ordered nematic phase.[15] Specifically, the electrostatic repulsion between rods were considered to be equivalent to an increase of the effective diameter with the excluded volume to be minimized if rods are parallelly packed. In such nematic phase the positional ordering entropy dominates over orientational entropy.[16] In chiral nematic LC phase, orientation of CNCs is governed by long-range interactions promoting their orientation combined with helical modulation. To date, there is no simple explanation of the origin of chirality in the CNCs assembly.[17,18] In Derjaguin- Landau- Verwey-Overbeek (DLVO) theory, generally, attractive van der Waals forces promote parallel organization but repulsive electrostatic forces- perpendicular organization of the particles.[19] Similarly to Stroobants - Lekkerkerker - Odijk (SLO) theory, both implement that inhomogeneous surface charge distribution results in particles twisting, i.e., chirality.[20] Others suggest that nanocrystals exhibit intrinsic twist by themselves, which arises from the chiral carbon atom in glucose unit constituting the backbones of cellulose. The nanocrystal twisted shape can also contribute to the formational of helicoidal morphologies as observed in bacterial and wood CNCs[21] and truncated

CNCs in aqueous suspensions.[22] Yet, theoretical results are frequently contradictory to those experimental. For instance, molecular dynamics simulations predict the twist to be continuous along the axis and not the alternative sharp twist change observed experimentally.[23,24]

As well known, cellulose nanocrystals, as well as other high-aspect ratio biomacromolecules (e.g., DNA fragments, cylindrical viruses, other polysaccharides) can form chiral nematic (cholesteric) LC phases in concentrated solutions.[25,26,27,28] For DNA, the strength of azimuthal correlations is expected to decrease at higher salt concentrations.[29,25,30] Direct measurements of intermolecular forces confirmed that energetically DNA cholesteric phase is controlled primarily by electrostatic interactions. The competition between electrostatic repulsion, the attraction between positively charged grooves of the molecules and negatively charged phosphate groups, and chiral electrostatic torque- can result in non-zero twisting angles validating the existence of cholesteric phase balanced by *electrostatic forces*.[31]

Yet, for CNCs those chiral assembly mechanisms are difficult to establish due to the assembly process being usually carried out across multiple scales (from nm- to micron scale, and further to macro-) and therefore, limiting the opportunity to reveal the holistic picture. Most of the studies focus on the final, assembled macro-state of the nanocrystals as monitored with optical microscopy and spectroscopy. The chiral nematic ordering of the cellulose nanocrystals starts in the solution state, upon nanocrystals entering the liquid crystalline phase during water evaporation with the processing conditions affecting the dynamics. For example, it has been observed that phase state and chiral pitch length depends on the CNC dimensions and surface chemistry, the suspension concentration[32], the ionic strength of the solution[33], temperature[34,35], and pH.[36] Changing CNC concentration and pH was shown to vary chiral nematic pitch length greatly.[12,36] Controlling the ionic strength of the CNC suspensions was shown to affect the phase separation in CNC suspensions and ordered phase formation.[36]

As known, capillary forces also play important role in the nanocrystals' assembly during drying process. Fast evaporation, for example, leads to polydomain films and a smaller pitch[37],[38] due to insufficient time allowed for tactoids with uniform pitch orientation to merge.[39] On the other hand, varying pH was shown to result in distortion of the chiral organization, therefore confirming the importance of the surface charging in the CNCs assembly process.[40] Alteration of the inter-crystal interactions by changing the solvent quality by reaching a higher ε_r (dielectric permittivity, such

as ε_r of water is 80) results in the blue shift of the light absorbance and leads to a decrease in pitch length.[41] On the other hand, decreasing the strength of the nanocrystals' Coulombic repulsion is reported to strongly decrease the pitch length[42,43], which can be attributed to decrease in effective nanocrystal volume and denser packing, however. The effect of surface charge has been previously addressed mainly with the regards on the phase separation and ratio existence of two phases (isotropic and anisotropic) and correlation between surface charge and the resulting chiral organization is not fully clarified. Majority of the studies of the abovementioned parameters, including those of particular interest in this work, pH and ionic strength, since they play critical role in electrostatic interactions, are conducted in suspension, in isotropic and liquid crystalline phases[44,45,46] with frequent focus on shear rheological properties.[32,47] Heterogeneous surface chemistry, shifting balance of intermolecular interactions, steric constraints and poly-dispersity of dimensions of formed aggregates, all conributes to the resulting organization. The balance of complex interparticle interactions, the attractive (van der Waals and hydrogen bonding) and the repulsive (Coulombic) controls nanocrystal aggregation.

The effect that Coulombic interactions have on the pitch distance in films is reported here, supported by observed shrinking in helical pitch and shifting of the photonic bandgap to a far UV-region from visible range (from 400 nm to 250 nm), increase in helical twisting power from 4 to 6 μm^{-1} and twisting angle, from 5.5º to 9°. We suggest that at Debye charge screening length below critical value of 3 nm results in loss of the long-range helical order and in transition to disturbed orientational order followed by disordered morphology at extreme ionic conditions. Subsequently, very high local orientation ordering with 2D orientation factor, S, reaching theoretical limit of 1 for ideal orientation (within 0.8-0.9) gradually decreased to random order with final S = 0.1-0.2. Additionally, the theoretical estimations suggest that with increase of the electrolyte's concentration, Coulombic forces dominance is overbalanced by the van der Waals forces and hydrogen bonding in the physical contact area during random contact in the suspension. Such balance shift promotes random nanocrystal organization and result in complete loss of chiral optical properties below critical Debye screening length of 3 nm.

The focus of this research is on careful quantitative characterization of molecular organization down to the level of individual nanocrystals and their orientational organization at nanoscale and microscale levels in terms of orientational order parameter in conjunction with interparticle

interactions in initial suspensions, usually overlooked in common observational research. In order to complete this markedly time-consuming careful derivation of these comprehensive molecular characteristics in conjunction with measurements of optical appearance, chiral activity, evaluation of charged state, we kept unchanged the processing conditions in this study and did not go across known intermediate stages of transition from isotropic suspension to solid state via LC state, a process widely studied with simple optical observation.

RESULTS and DISCUSSION

I. Experimental

CNCs studied here were isolated from wood pulp by acid hydrolysis according to the established protocol.[48] Briefly, 5 g of dried wood pulp pieces were added to 95 g of 64 wt.% sulfuric acid solution at 45°C and stirred continuously for an hour. To quench hydrolysis, the reaction solution was poured into a glass container of tenfold acid volume ultrapure water. The suspension was left overnight to let it phase separate and then, the bottom layer was decantated and centrifuged for 10 min at 6000 rpm in order to wash the CNC solution.

After washing steps, the supernatant was removed, ultrapure water added, and the CNC solution was dialyzed against water until pH was neutral. In order to obtain homogeneous and well-dispersed suspension everywhere, the resulting suspension was centrifuged again at 10,000 rpm and then tip-sonicated at 40% amplitude, 5 s on/5 s off, for 4 min and 30 sec using a large tip sonicator (Qsonica Q125 with 1/8" diameter probe). To prepare CNCs with different electrolytes' concentrations, first, sodium hydroxide in pellets (Millipore Sigma) was dissolved in water and then added controllably to 1wt.% CNCs dispersion so that the final concentration of NaOH was in the range from 0.1 to 10mM; higher concentrations resulted in gelation. Such electrolyte concentrations are typical for CNC suspension studies.[49,50] MilliQ water (18.2 MΩ•cm) was used for all the experiments. CNC films were obtained via evaporation-assisted self-assembly (EASA). Suspension with different electrolyte's concentrations were placed into Petri-dishes and allowed to form solid films under slow drying conditions identical for all specimens studied here. Specifically, 10 mL of each CNC solution was drop cast onto Petri dish (diameter 5 cm). The water was allowed to evaporate under ambient conditions (23°C, 30-40% RH). Finally, thin CNC films were formed within two days and their thickness was measured to be around ~50 ± 20 um. For simplicity, further in the paper, the films obtained from the CNC suspension containing XmM of

NaOH will be referred as XmM CNC film (for example, the film obtained from 5mM NaOH CNC suspension is called 5mM CNC film).

As-prepared suspensions were allowed to stabilize overnight and then *zeta-potential* was measured with Zetasizer Nano ZSP (Malvern Instruments) in polystyrene cuvettes. The ζ-potential is derived from the electrophoretic mobility of the CNCs, which was determined from electrophoretic light scattering (ELS). The hydrodynamic apparent particle size of dispersed CNCs was measured by *dynamic light scattering (DLS)* using a Zetasizer Nano ZSP (Malvern Instruments) equipped with a red laser (633 nm) under a backscatter detection angle of 173°. The harmonic intensity-weighted average particle diameter (z-avg) was obtained after equilibration for 30 min at 25 °C. *Optical microscopy* was performed on OLYMPUS optical microscope equipped with polarizers and in dark-field mode. *Circular dichroism* measurements were performed on AP Chirascan™-plus CD Spectrometer with films mounted on the sample holder with empty middle space perpendicularly to the beam path in a wavelength range between 200 and 800 nm.

The chiral anisotropy factor, g_{abs}, for chiral nematic films was obtained from spectroscopic measurements under different circular polarization by using the equation (Eq. 1) [51,52,53]:

$$g_{abs} = \frac{\Delta A}{A} = \frac{\theta}{32980 \times A} \qquad \text{(Eq. 1)}$$

where ΔA is absorbance difference between left and right circularly polarized light at the CD peak, A is absorbance at the CD peak, and θ is ellipticity from CD spectra in mdeg unit, respectively.

UV-Vis spectroscopy was done using a Shimadzu UV-3600 Plus UV-Vis-NIR Spectrophotometer with a range of 185 to 1000 nm. All measurements were run in quartz cuvette three times , and performed on at least 3 films, and finally averaged. *ATR-FTIR* was performed on Bruker Vertex 70 instrument with a range of 4000 to 1200 cm^{-1} with 2 cm^{-1} resolution. Different suspensions were drop-cast onto ATR crystal and then FTIR spectra were recorded.

AFM images were obtained on the Dimension Icon microscope (Bruker) in the light tapping mode in air with 1024x1024 pixels resolution with AFM tips of radius ~5 nm according to usual procedure in order to maximize resolution and reduce surface damage.[54] CNC suspensions were drop cast onto freshly piranha treated silicon wafers. All AFM images were flattened in NanoScope software and transferred for further fine orientation order analysis and calculations of orientational order parameter with GTFiber software.[55] This software was applied for calculation of cellulose

nanocrystals orientation map and azimuthal distribution as well as evaluation of 2D Herman's order parameter, S. Examples of the image analysis can be found in Supplementary Information for all specimens and discussed further for selected examples.

SEM images were taken on Hitachi SU-8230 Electron microscope operated at 3kV voltage. Films were cut with clean razor blade and then attached perpendicularly to the SEM mount. Samples were sputter-coated with gold for 45 sec at 30 mA (resulting gold layer thickness ~3nm).

II. Suspensions of CNCs and their properties

In this study, we chose to introduce sodium hydroxide (NaOH) into the suspension, since both pH and ionic strength influence electrostatic interactions and pH affects the competition between van der Waals and electrostatic repulsion between nanocrystals.[56] Overall, addition of the electrolyte, sodium hydroxide (NaOH, in water), into CNCs dispersion leads to decrease in electrical double layer thickness of individual nanocrystals, and, thus, reducing the range of repulsive interactions, which might result in attraction forces dominance in the course of assembly as is explored in this study. We avoided usage of the NaCl in order to exclude any possibility of the salting-out effect, reported for this common electrolyte that interferes with high-resolution AFM analysis. Salting out effect tends to decrease solubility of the colloids in water with higher electrolytes concentration and was reported to be the lowest for OH^- anion and Na^+ cation.[57]

Previously, it has been shown that cellulose nanocrystals phase behavior depends on the nanocrystals aspect ratio[58], surface chemistry[64], and surface charge density.[59] Taking this into consideration, in this study, we kept all the above-mentioned parameters constant by using identical conditions for CNCs obtained from the same batch. Additionally, to make sure that sulfate half ester groups remained undisturbed on the surfaces of the CNCs with electrolyte addition, we took the 10mM NaOH suspension (zeta potential measured -25.4 mV) and performed dialysis on it for 24 hrs, to reverse the ionic strength, e.g., removed Na^+ ions. Indeed, after this treatment, zeta potential increased to -41 mV, which is identical to the pristine (0mM NaOH) CNC suspension that had zeta potential of -39mV (Fig.S4).

As-prepared CNC suspensions with sodium hydroxide concentrations of 0.1mM, 0.5mM, 1mM, 5mM and 10mM were homogeneous in the appearance (Fig. 1). Only in the case of 5mM and 10mM electrolyte's content, the suspensions appeared slightly opaque, however, no gelation was

observed even after long storage. Since the CNC concentration was lower than critical LC formation concentration, electrolyte's addition did not cause any aggregation and the suspensions were clear and isotropic.

Diluted suspensions did not display any birefringence between cross-polarizers indicating that LC phase was not presented (Fig. S1). Considering that CNC with electrolyte concentration above 10 mM promoted gelation in suspension due to excessive nanocrystal aggregation and formed fully disordered structures in completely transparent films after full drying, we limited our studies to 10 mM electrolyte concentration.

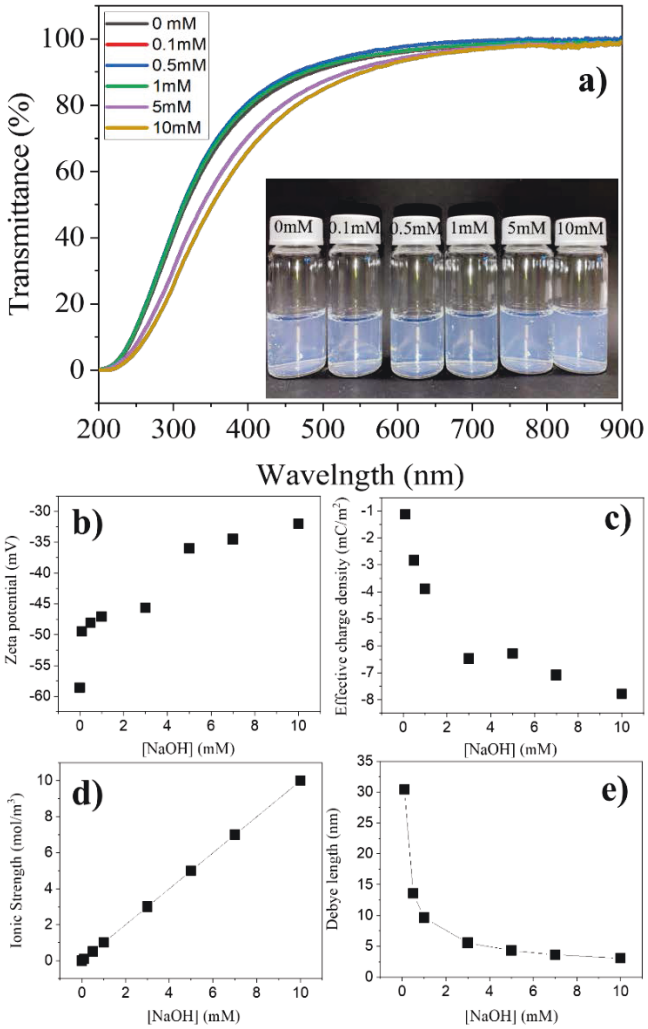

Figure 1. Transmittance spectra of cellulose nanocrystal suspensions with different electrolyte concentrations. The inset shows vials with as-prepared CNC suspensions. (a) Zeta potential (b) of CNC suspensions as a function of NaOH concentration and corresponding calculated characteristics: surface charge (c), the ionic strength (d), and Debye charge screening length, λ_D (e).

The UV-vis transmittance spectra exhibited no absorption peak in the visible region confirming isotropic nature of the prepared dispersions (Fig. 1). For the electrolyte concentration up until 5 mM, the transmittance curves of the dispersions were identical showing transmittance above 80% above 350 nm wavelength (Fig. 1). For higher electrolytes' concentrations, light transmittance decreased to 60% due to the increasing CNC aggregation that causes excessive light scattering and appearance of weak opalescence without, however, anisotropic and birefringent LC phase formation (Fig. S1).

Upon electrolyte's addition, zeta potential gradually decreased from -58mV (at 0 mM) to -32mV (at 10mM) (Fig.1b). This zeta potential is sufficient to stabilize the dispersion and keep it stable for months of storage (Fig. S6). The ionic strength of the solution increased with increasing electrolyte's concentration to 10 mol/m^3, resulting in effective surface charge density increasing dramatically from -1 to -8 mC/m^2 as it scales exponentially with nanocrystals surface potential (Fig. 1c, d, see Eq. S7). In the remainder of the paper, we will use the term 'increase' when the effective charge density becomes more negative referring to the absolute magnitude of the potential. Effective charge density describes the charge density in electrical double layer of the individual CNC and increase in the value should be considered to proportionally decreasing the capacitance of the electrical double layer (EDL).

As known, Coulombic-driven behavior of the particles in solution is governed not only by the particle's surface charge properties, but also but its microenvironment. This is mainly characterized by zeta potential, and the outmost layer that will determine interactions between two nanoparticles in solution, which is described by the effective surface charge density.[60] Therefore, to estimate the charge changes upon electrolyte addition, we calculated the effective surface charge density via Gouy-Chapman equation (see SI).[61,62] Effective charge density related to the outmost layer in solution and usually is scalable with the surface charge density of the colloids.[61]

Addition of the electrolyte affects solvent's ionic strength and the Debye charge screening length, which are related according to the equation:

$$\kappa^{-1} = \sqrt{\frac{\varepsilon_r \varepsilon_0 k_B T}{2 N_A e^2 I}} = \frac{1}{\lambda_D} \qquad (2)$$

where I is the ionic strength of the electrolyte (mol/m^3), ε_0 is vacuum permittivity, ε_r is permittivity of the media, $\lambda_D$is the Debye charge screening length, k_B is Boltzmann constant, T is temperature, N_A is the Avogadro number and e is the elementary charge.

The increase of the effective negative charge density as calculated from eq. S7 is a direct result of the surface absorption of sodium ions (Na^+) and consecutive shrinkage of the electrical double layer (Fig. 1c). Correspondingly, Debye charge screening length, which is directly related to EDL thickness, decreased ten times from 30 nm (at 0.1 mM) to 3nm (at 10 mM) (Fig. 1e) that falls in the range of 1-100 nm common for various colloidal nanostructures.[63] After calculating these charging characteristics, we considered the organization of thin films fabricated from different suspensions as discussed below.

Optical properties and morphology of thin films

Thin CNC films obtained from suspension with lower electrolyte concentration (up to 5 mM) showed vivid iridescent color indicating formation of chiral nematic organization after complete drying (Fig. 2a-d).[12,64] As known, the characteristic fingerprint texture observed in dark-field optical images indicates the formation of the helical chiral nematic morphology with selective light reflection within individual tactoids.[65] The films did not demonstrate visible difference in their iridescence up until the electrolyte's concentration reaching 5mM. At 5mM concentration, the resulting film turned out matt and opaque, although still showed light blue coloring but no clearly defined tactoids (Fig. 2e, k). At last, 10 mM CNC film was colorless and transparent suggesting complete loss of chiral nematic organization (Fig. 2f, l).

Cross-sectional SEM images of the films showed differences in films internal organization, 0.1 mM CNC film exhibited well-defined layered texture, a characteristic Bouligand morphology for chiral nematic organization propagating through the entire film thickness.[66,67] Interestingly, cross-sectional SEM of the 10mM film showed various layered structures. For 10 mM CNC film, Bouligand structure was no longer present, as layers lost the "wave" pattern observed for the cross-section of twisted Bouligand structure, in the case of 10 mM film the layers were stacked on top of each other like lasagna sheets (Fig. 2m,n, Fig. S11). As is further supported by the AFM (see below), loss of local order within each layer results in loss of global chiral nematic organization, and the formation of highly disordered nematic layers (Fig. S10).

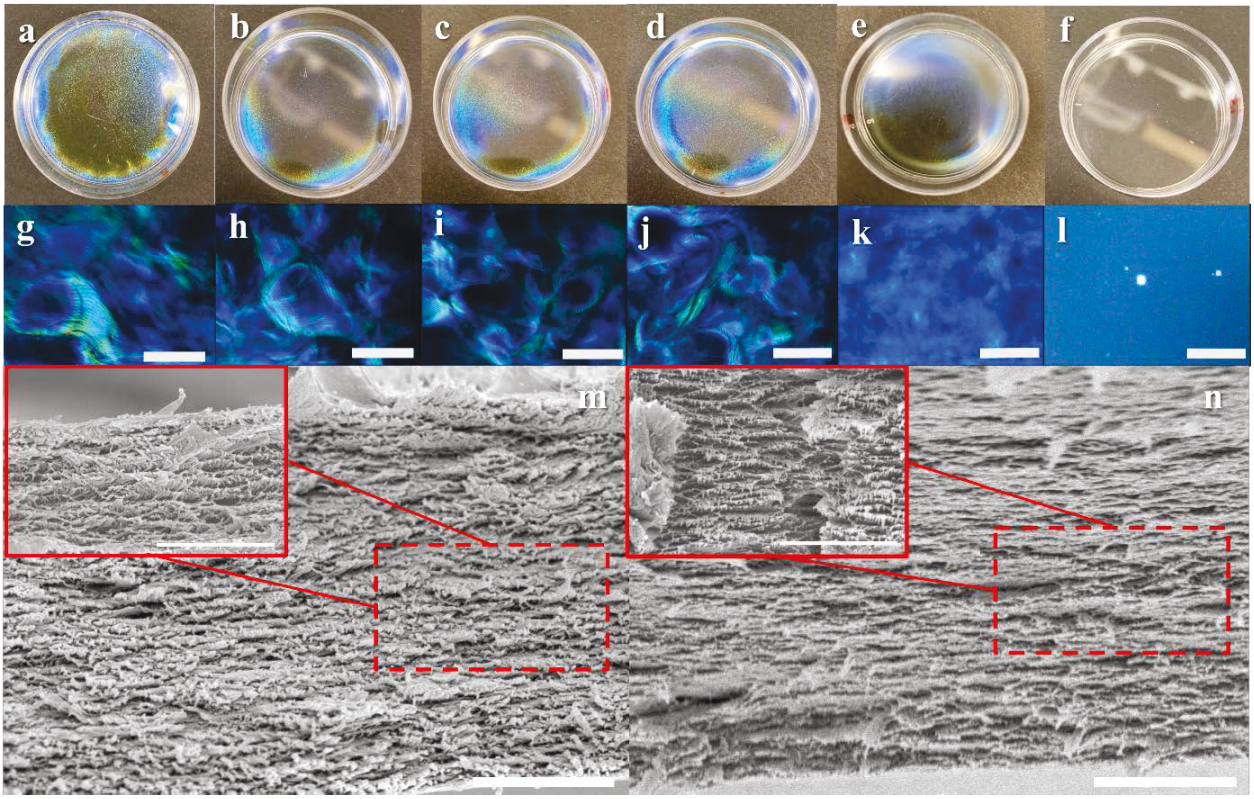

Figure 2. Photographs of the CNC films obtained by solvent evaporation assisted assembly CNC suspensions at different electrolyte concentrations: 0 mM (a), 0.1 mM (b), 0.5 mM (c), 1mM (d), 5mM (e), 10 mM (f) and corresponding dark-field unpolarized optical microscopy images (g-l), scale bars are 75 um for all images, Petri dish diameter is 5cm. Films thickness is ~50 ± 20 um. SEM images of the cross section of 0.1 mM CNC film (m) and 10 mM CNC film (n), scale bars are 1.5 um, insets (solid red boxes) are zoomed in images with scale bars of 1um. SEM images were collected at an angle to visualized layered morphology.

AFM images revealed internal organization of these films to be very different confirming transition from ordered chiral nematic organization to completely disordered organization (Fig. 3, S2). At larger surface areas, uniform orientation of the nanocrystals with gradual bending of the director and occasional characteristics microscopic defects for chiral nematic phases was observed for all films below 5 mM (Fig. S2).[68] The excessive attraction forces will cause cellulose nanocrystals to aggregate, which is not favorable for chiral nematic structure formation. In order to form chiral structure, it was shown that CNCs form tactoids that, if allowed enough time, will merge and produce well organized chiral structure.[69] Yet, for the most part, these tactoids are randomly packed in the final thin film. Therefore, for CNC films (3D order parameter) with SAXS or XRD methods showed bulk orientation order parameter below 0.1.[70,71,72] Preferred orientation with shearing [72] or magnetic field [73] allows determination of 3D orientation order parameter closer to

those expected for organic LC phases, 0.5-0.8, indicating relatively uniformly oriented tactoids. On the other hand, AFM for thin films is the best technique to representatively observe how individual nanocrystals and their bundles pack in each layer, and therefore, evaluate true orientation order at microscopic level unaffected by larger scale defects and tactoids disorientation (Fig. 3). However, to date no such quantitative molecular-level characterization has been systematically conducted and reported for thin CNC films.

In order to quantify the nanocrystal reorganization, we calculated 2D Herman's orientation order parameter from azimuthal distribution of director as averaged over microscopic surface areas of the individual monolayers (Fig.4, S3). It is important to note that 3D bulk orientation order parameter determined in literature from scattering and polarization methods differs from the local 2D orientation order parameter from AFM images discussed here. It is worth to note that 3D order parameter (found in literature) is the average number obtained from entire volume[70] and is relatively lower, due to the random orientation of the microscopic domains (tactoids), and thus should not be directly compared with localized analysis conducted here. In fact, 2D orientation order parameter provides direct quantitative characteristics relevant to true molecular-scale orientation correlation of individual nanocrystals and their bundles within an individual tactoid unaffected by their macroscopic orientation within the entire volume of the films.

Higher resolution AFM images capable of resolving individual nanocrystals and their bundles with sufficient quality (below 1 nm per pixel) can be collected at microscopic surface areas at multiple locations (Fig. 3, S3). These images showed that individual nanocrystals bundles are uniformly oriented across several micrometers surface areas with very few local defects and high uniformity in nanocrystal orientation (see below) (Fig. 3, top row).

With further increase of electrolyte concentration to 1mM, microscopic defects with correlated changes in reorientation of nanocrystal bundles became apparent in CNC films (Fig. 3). In 5 mM CNC film, nanocrystals lost their long-range parallel orientation and were aggregated within submicron domains of oriented bundles separated by disordered defects. Finally, in the case of the 10 mM film, AFM revealed random orientation and organization of the limited nanocrystal bundles separated by larger pores (Fig. 3f). At this electrolyte concentration, the surface texture became randomized with numerous disordered textured domains and pinhole defects as observed across large surface areas (Fig. S2).

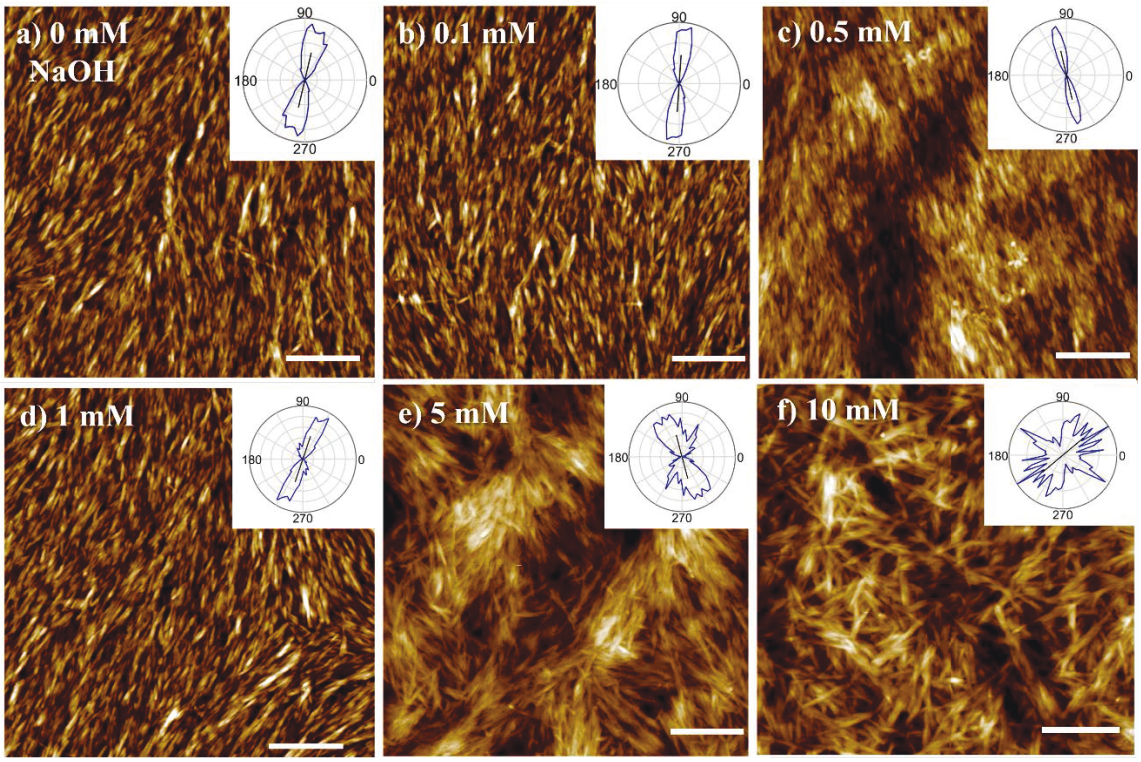

Figure 3. AFM topography images of the CNC films from suspensions with different electrolyte's concentrations: 0mM (a), 0.1mM (b), 0.5mM (c), 1mM (d), 5mM (e) and 10mM (f) and corresponding azimuthal distributions of nanocrystal orientations. Scale bars are 400 nm.

As has been discussed above, in order to quantify the orientation order at molecular scale, azimuthal distribution of the nanocrystal axes, and 2D orientation order parameters, S, were calculated for all films (see details in Supplementary Information with examples for all CNC films studied here, Figure S3). Examples of the AFM image and corresponding orientation analysis are presented in Figure 4 for two extreme cases of CNC films cast at 0 mM and 10 mM electrolyte concentrations.

Computational analysis re-vectorizes the nanocrystal orientation and yields and orientation map across the selected surface area that reflects the statistics of orientational organization of the cellulose nanocrystals.[55] The separation of the cellulose nanocrystals from background allows to visualize individual nanocrystals and their bundles at high spatial resolution achieved in this study and azimuthal angle distribution are represented by different colors (note color-coded mapping in right-bottom corner in Fig. 4c and f). The orientation distribution is characterized by integrated

azimuthal distribution across the selected surface area with central line indicating their average orientation across the entire image (Fig. 4b, e).

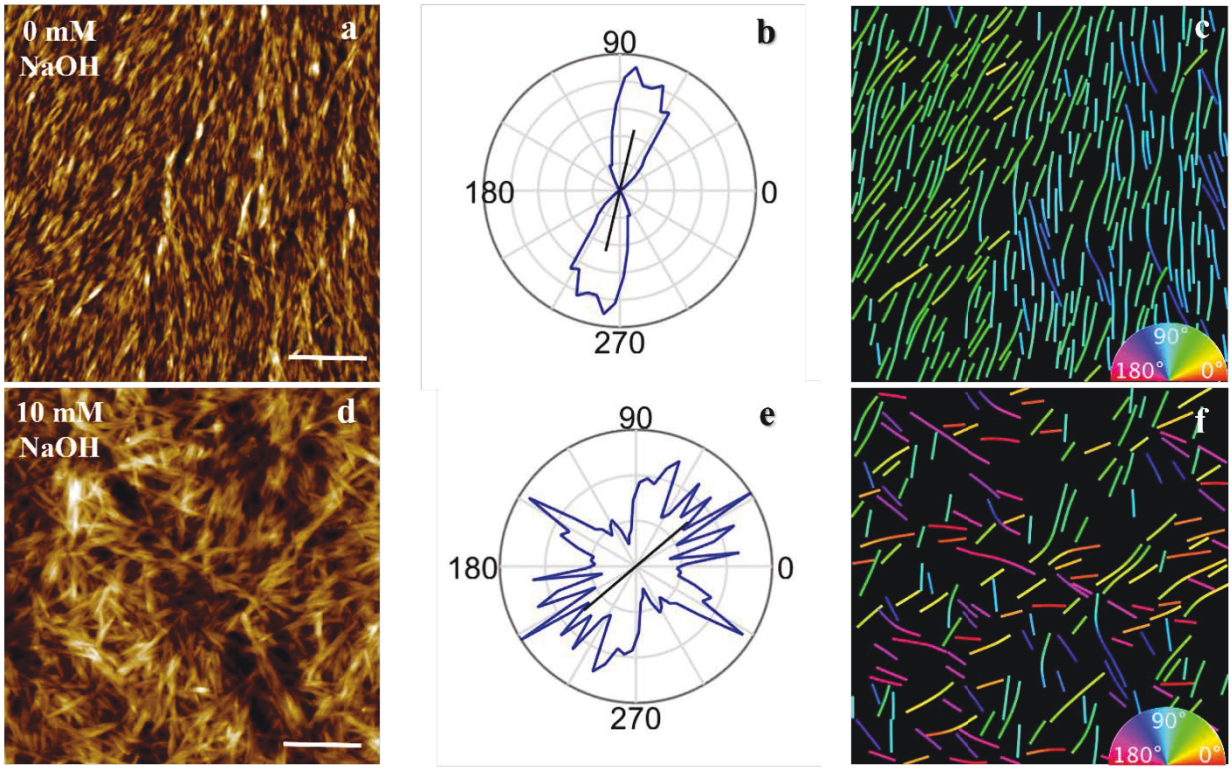

Figure 4. GTFiber analysis results for the AFM image of the thin films of CNC suspensions containing 0mM (a) and 10 mM (d) NaOH, orientation distribution for 0 mM (b) and 10 mM (e), and False color Orientation map extracted from the original AFM images of 0 mM NaOH (c) and 10 mM NaOH (f), inset-color map for the nanocrystals' orientation angle. Scale bars are 400 nm.

Azimuthal distribution with narrow two-leave shape indicates uniform distribution along unidirectional orientation (Fig. 4b) and multiple azimuthal peaks at various angles indicate random orientation of individual nanocrystals (Fig. 4e). Such orientational distribution analysis allows for unambiguous quantitative analysis of the AFM images that cannot be derived from conventional analysis of the original images (e.g., surface microroughness, phase variation, nanocrystal dimensions) previously reported.

Furthermore, analysis of the azimuthal distribution allows for the calculation of the 2D orientation order factor as: $S_{2D} = 2 < cos^2\theta_n > -1$, where θ_n is the angle between an individual nanocrystal and the overall director, n, which is chosen as the average orientation of the total nanocrystal population. Theoretically, perfectly organized structure will have order parameter of 1, and completely random structures possess S closer to 0, and common range of orientation order is

within 0.6-0.8 for various LC media with, however, all current results employing 3D orientation order parameter (see discussion above).[74]

Returning to the image analysis of the two extreme cases, it is important to note that very narrow azimuthal distribution was observed for all films obtained from suspensions with low electrolyte concentration (below 1 mM) with the average deviation of the azimuthal angle around 10° ± 5 (Fig. 3, 4). In contrast, 1mM CNC films, show wider azimuthal distribution, which starts adapting multi-loop shape indicating presence of the surface areas of differently orientated nanocrystals especially visible for 5 mM CNC films (Fig. 3d, e). Finally, nanocrystal azimuthal distribution for 10 mM CNC films becomes totally isotropic with numerous spikes reflecting random local orientation of isolated nanocrystals and their bundles (Fig. 3f). This azimuthal distribution for these films indicates that there was no preferred orientation of nanocrystals across the whole image with multiple local orientations within separated domains (Fig. 3f inset).

To quantitatively compare the nanocrystal alignment behavior in the series of CNC films, orientation order parameter S as a function of NaOH concentration is presented in Fig. 5. It is apparent from these data, orientation order parameter decreases consistently with increasing NaOH concentration. Values of S_{2D} are at very high level of 0.8 to 0.9 for low electrolyte concentrations below 1 mM reflecting highly correlated and uniform orientation of nanocrystals within microscopic domains of chiral nematic organization, which is in good agreement with previously reported data for 3D orientation order parameters for various CNC films.[75,76,77,78]

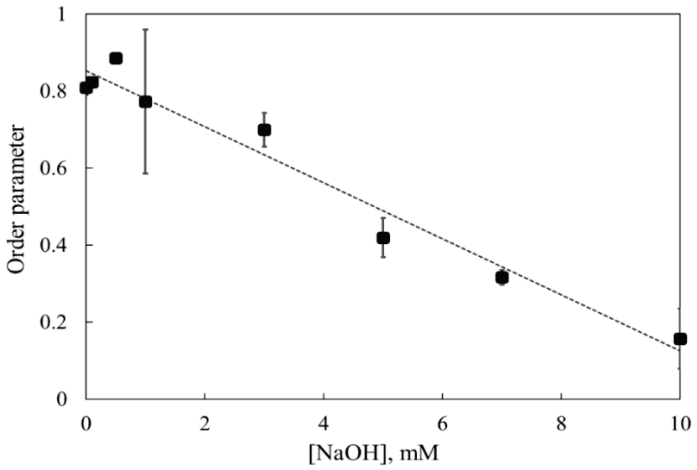

Figure 5. Orientation order parameter for CNC films obtained from suspensions with different electrolyte concentrations. For each point, at least three AFM images from three different surface areas were analyzed.

Upon addition of electrolyte to suspension, the orientation order parameter steadily decreased, and at the concentration of 5mM reached the level of 0.3-0.4, which is considered to be the threshold value for the orientation order parameter of a nematic phase (Fig. 5).[79] Finally, for 10 mM CNC films, orientation order parameter approached the level for random orientation order (around 0.2). Such level quantitively confirms local random orientation of the nanocrystals on the surface of CNC films obtained at the highest ionic strength. [80]

We further analyzed the optical behavior of the CNC films beyond apparent optical iridescence in Fig. 2 by measuring UV-Vis transmission spectra (Fig. 6). The CNC films obtained at low electrolyte concentration, below 5 mM possessed well-defined absorbance peak within 250 to 400 nm (Fig. 6). Increasing NaOH concentration resulted in significant blue shift. The peak exhibited by the 5 mM film was less defined, although still observable but the 10 mM CNC film spectrum appeared rather featureless. The case of the 10 mM CNC film we will further consider as 'border case', based on the optical microscopy images, visual appearance and SEM images of the film's cross section the structure does not meet the threshold to consider it chiral, however, the shoulder on the UV-vis spectra that potentially could appear due to presence of the layered structure was taken as peak position for calculations.

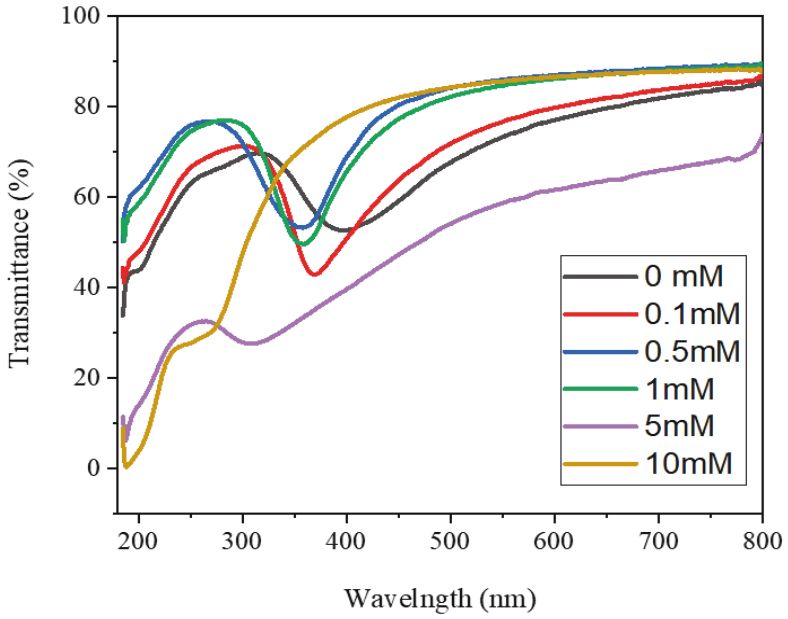

Figure 6. Transmission UV-Vis spectra of the CNC films with different electrolyte content.

Furthermore, from UV-vis spectra, we calculated important structural characteristic parameters, such as pitch length, P, helical twisting power (HTP) and twisting angle per monolayer, Θ vs NaOH concentration (Fig. 7). These characteristics have been derived as discussed below.

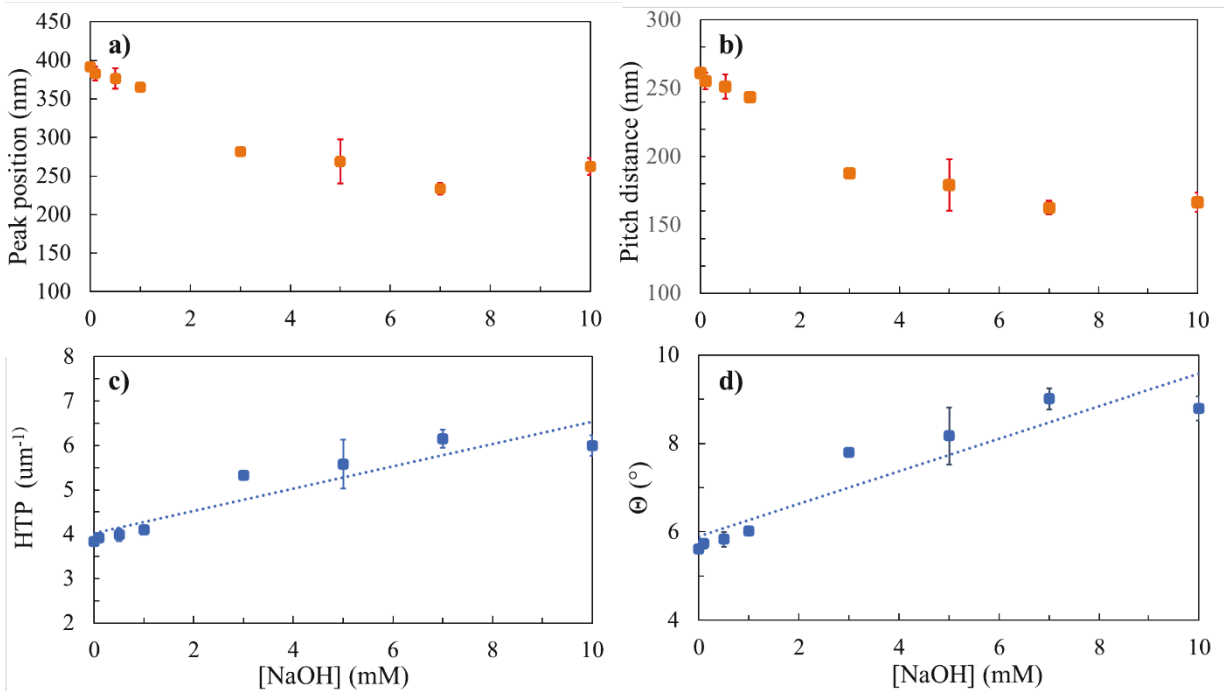

Figure 7. Reflectance peak position of different CNC films (a) and corresponding pitch length (b), helical twisting power (c) and twisting angle per monolayer (d) of the CNC films vs electrolyte's concentration. The experiments were conducted at least three times on the films dried from different CNC batches. Although it is known that CNC properties may vary from batch to batch, trend is consistent, as reflected in modest error bars. The error bars values can be found in Supporting information (Table S3).

First, the preferable wavelength of the reflected/absorbed light is related to the chiral pitch length according to the relationship[14] :

$$P=\lambda/n_{ave}\cos\theta \qquad (3)$$

where λ is the peak position, n_{ave} is the average refractive index (n_{ave}=1.5 for CNCs [81]) and θ and the angle between the surface normal and the incident ray.

Next, helical twisting power (HTP) can be calculated to describe the chirality trend of the individual nanostructures.[82,83] The HTP can be calculated from pitch-composition data as the slope of the inverse change in pitch distance, using the equation: [84]

$$\mathrm{HTP}=(Pc_w r)^{-1} \qquad (4)$$

where, c_w is the concentration of the CNCs (1wt%) and r is enantiomeric purity (r=1 for CNC). Finally, the twisting angle per monolayer, θ, can be calculated from the common equation by using the pitch length and monolayer thickness:[82,85]

$$\theta=\frac{360d}{P} \quad (5)$$

where *d* is the effective monolayer thickness, around 4.1 nm for CNC films studied here (taken as nanocrystals diameter calculated from the AFM image of the individual nanocrystals (Fig. S5)).

As calculated with these equations, the pitch length gradually dropped from over 250 nm to below 200 nm with increasing electrolyte concentration to 5mM (Fig. 7a, b). Further addition of electrolyte resulted the loss of well-defined light absorption peak well in agreement with observed iridescence loses (Fig. 2). Next, helical twisting power and twisting angle increased gradually across all electrolyte concentrations (Fig. 7c,d). HTP for pure CNC suspension (0mM NaOH concentration) was found to be 4 um^{-1} and did not increase significantly until electrolyte's concentration reached 5mM. At 5 mM, HTP was 5.5 um^{-1} and it reached 6um^{-1} for higher electrolyte concentrations (7 and 10 mM). The same trend was observed for the twisting angle per monolayer: at 0mM concentration, twisting angle was around 5.5° and stayed in this range until electrolyte's concentration did not reach 1 mM. At higher electrolyte concentration, θ gradually increased and reached the highest value of 9° for higher electrolyte's concentrations (at 7 and 10 mM). Again, in the case of 10 mM CNC film, the chiral structure was not clearly observed but the above-mentioned characteristics were still calculated assuming that the shoulder peak in the UV-vis spectra appeared possibly due to residual layered structures in some regions.

The decrease in pitch length suggests that the individual nanocrystals pack at higher twisted angle between nanocrystal axes (Scheme 1). On the other hand, such twisting causes decrease in the effective physical contact area between nanocrystals (Scheme 1). Dramatic decrease in the contact area below some critical values, might compromise the ability of the nanocrystals to maintain close-to-parallel packing with correlated minor twist thus limiting the ability to form correlated packing leading to helical organization as will be discussed below. Finally, it is worth to note that FTIR spectra for all CNC films confirm that the inter- and intramolecular hydrogen bonding networks in films obtained under different electrolyte concentrations were not disrupted by changing ionic conditions (Fig. S9, Table S2).[86,87,88]

Circular dichroism of CNC films as reflection of chiral organization

In addition to dimensional characteristics of chiral nematic organization discussed above, we measured circular dichroism of the CNC films to monitor the light polarization for different optically active films (Fig. 8). As clear from these spectra, intense positive CD peaks is observed for all CNC films obtained from suspensions at electrolyte concentration below 5 mM with peak position exhibiting blue shift in synchrony with pitch length decrease. This CD signal confirms expected left-handed helicoidal organization. In addition, blue shift is accompanied by peak broadening and decreasing intensity at 5 mM until disappearance at the highest (10mM) concentration (Fig. 8).

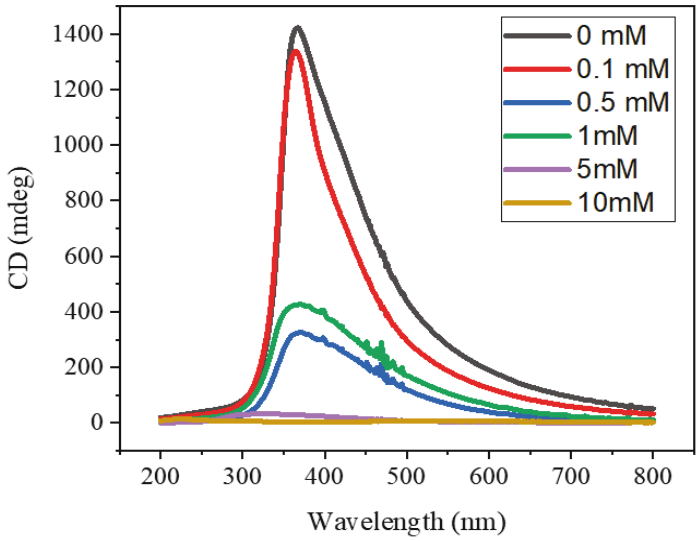

Figure 8. CD spectra of the CNC films with different electrolyte concentrations.

Moreover, for all CNC films, we calculated the dissymmetry factor, known as g-factor, which is an indication of degree of chiral structure activity in reflecting left and right circular polarized lights and calculated as the difference in the intensity of left- and right-polarized light absorbance (see methods for details).[89] From these calculations, we observed that g-factor decreased more than ten times from very high value of 1.0 (for pure CNC film without electrolyte) to 0.04 for the 5mM CNC film (Fig. S8). For the 10 mM CNC film g-factor drops to near zero, close to background values, $2x10^{-4}$, confirming untwisting of the helicoidal organization as concluded from microscopic and spectroscopic measurements discussed above (Fig. S8). Note that despite the g-factor for traditional biological chiral systems known to be low, the value of $2x10^{-4}$ is very low for common CNC films and is close to the spectrophotometer sensitivity, especially considering

extreme broadening and far UV position of the CD peak (Fig. S7). Next, we consider how changes in interparticle interactions derived from primary charged states can be related to and explain structural transformations discussed in previous sections.

Nanocrystal organization and interparticle interactions

Next, we will discuss how observed and confirmed changes in orientation ordering and optical properties can be related and explained by the variation of the interparticle interactions. As known, total interparticle interaction energy U(h) between rod-like particles, can be presented as the sum of the attraction forces $V_a(h)$ and repulsion forces $V_r(h)$, according to:[90]

$$U(h) = \mathrm{Va}(h) + \mathrm{Vr}(h) = 64nk_bT\gamma^2S\kappa^{-1}e^{-\kappa h} - \frac{A}{12\pi h^2}S \qquad (6)$$

where n- is the number density of ions in the medium, k_b – is Boltzmann constant, T is the temperature, $\gamma = ze\Psi/k_bT$ (e is the elementary charge and z is the valency of the ions in solution), Ψ is the surface potential, S is surface area of the rod, κ is the inverse Debye charge screening length, A is Hamaker constant and h is the separation distance (see SI for details).

First, the calculated repulsive energy vs distance between nanocrystals drops dramatically with increasing electrolyte concentration (Fig. 9a). On the other hand, the calculated attractive energy showed very modest changes across all electrolyte concentrations (Fig. 9b). Finally, the total energy shows common potential barrier around 5 nm with fast drop at shorter distances (Fig. 9c).

Overall, higher electrolyte concentration decreased the potential energy barrier dramatically and the barrier was completely suppressed at 5 mM making attraction forces dominant at any distances between nanocrystals (Fig. 9c). Correspondingly, the experimentally derived Debye charge screening length drops to below 5 nm in the same range accompanied by increase in effective charge density and significant increase in ionic strength (Fig. 1c-e). In addition, the shift in the repulsive energy shows us that the energy barrier is not only reduced due to shrinking of electrical double layer thickness (left shift of the curve), but also by lowering particles charge (down shift of the curve), confirming synergistic effect of the ionic strength in suspension and charge density of nanocrystals on integrated interparticle interactions. Certainly, self-assembly of the CNCs is affected by several interactions: van der Waals forces, electrostatics, hydrophobic interactions, hydrogen bonding, therefore, we cannot claim that that the resulting chirality is a direct consequence of the long-range Coulomb forces. Yet it is remarkable that our results can describe

qualitatively and quantitatively chiral organization of the CNCs based on the electrostatic interactions alone as supported by DLVO theory.

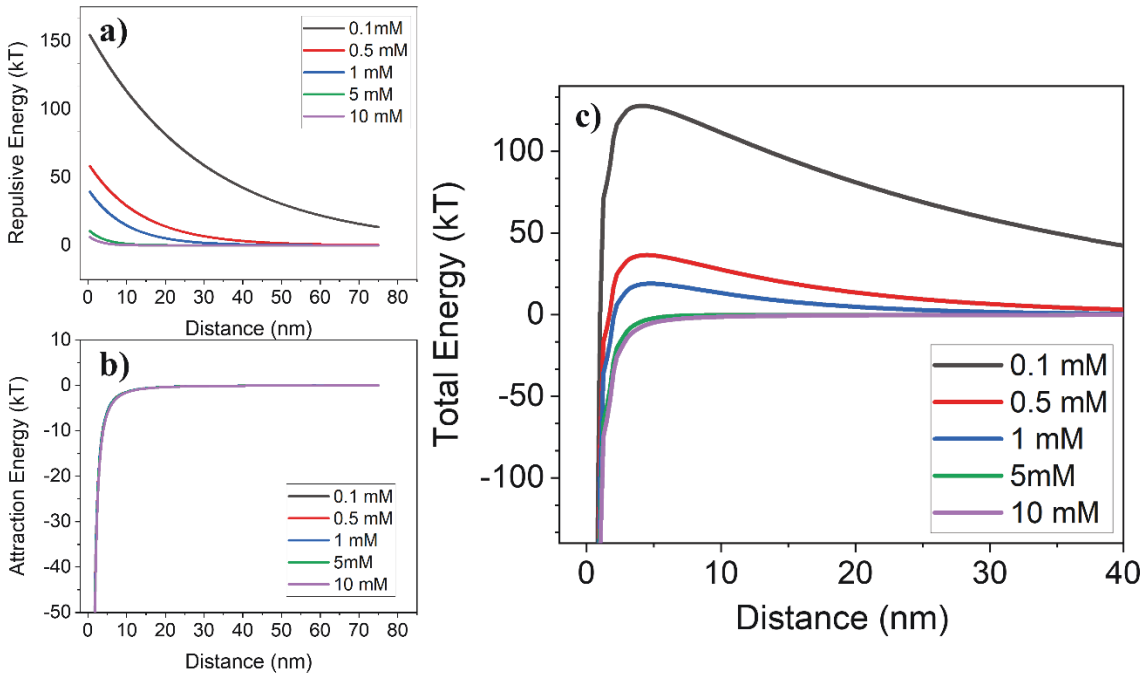

Figure 9. Repulsive Coulombic energy (a); attraction van der Waals interaction energy (b); and total potential energy of interaction (c) between two cellulose nanocrystals obtained from DLVO theory and plotted as a function of interparticle distance.

CONCLUSION

The question if Coulombic interactions can control chiral organization beyond other physical factors such as twisted shape and surface group chirality is frequently debatable. As we have discussed above, the variation in the solvent ionic strength results in dramatic changes of the effective charge density and electrical double layer thickness measured experimentally (Fig. 1) and interparticle interaction energy calculated from DLVO theory (Fig. 9). We take into consideration the limitations of the DLVO theory and its applicability to describe high aspect ratio nanocrystals minute orientation-dependent interactions until they start twisting. In fact, minute misalignment of nanocrystals during initial random contact in solution creates complex, heterogeneous energy landscape with counter-balanced trends of different contributions. Thus, we suggest empirical model of the assembly process that take into account our detailed quantitative

characterization of local orientation ordering of nanocrystals and its variation revealed in this study (Scheme 1).

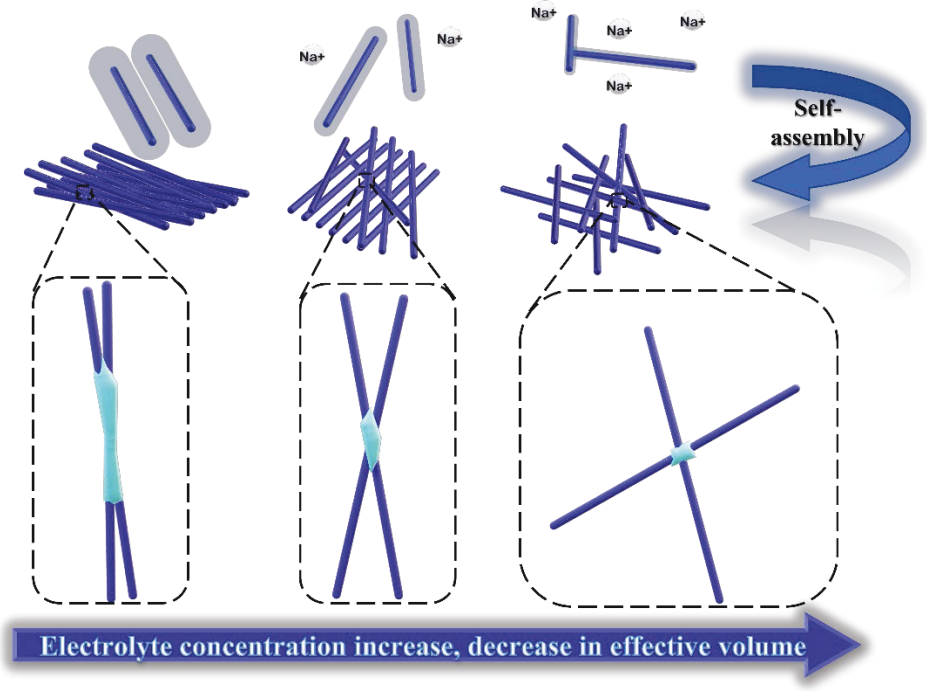

Scheme 1. Suggested assembly of individual nanocrystals with different effective charges in the suspension and during aggregation (top) and preferential packing of nanocrystals in different scenarios from parallel packing to misaligned nanocrystals and further to random organization with local cross-packing (from left to right). Light blue areas show evolution of the physical contact area during initial misaligned contact.

First, by absorbing the counter ions from the bulk, the increase of the effective charge density of cellulose nanocrystals results in decrease in electrostatic layer capacitance and therefore leads to its gradual shrinkage. We suggest that effective reduction in effective Debye charge screening length leads to short-range attraction forces dominance in local contact area upon initial contact in solution, and such counter-balanced interaction variation can explain the resulting gradual untwisting of nanocrystal orientation ordering observed here. Overall, lower Debye charge screening length promotes direct intimate physical interaction in the limited contact area between two neighbor nanocrystals in un-favorable non-parallel contact during random bumping in diluted suspension of high aspect ratio nanocrystals.

Secondly, concurrent increase in surface charge density causes reduction of the facet-to-facet interactions that will promote small, controlled twisting in nearly co-aligned nanocrystals (Scheme 1). Thus, contribution of direct physical contact into twisted arrangement between two neighboring

nanocrystals along with increased repulsion between the separated ends of nanocrystals, far from the contact point, force them to twist more, effectively increasing twisting power and twisting angle and, eventually, reducing the pitch length (Fig. 7).

Finally, at high electrolyte concentrations, drastically diminishing effective contact area and stronger repulsions between misaligned nanocrystal portions far from the contact area causes complete loss of the ability for correlated twisting, compromise parallel twisted packing of nanocrystals, and, eventually, destroy the helicoidal organization at larger scale (Scheme 1). The resulting distraction of the orientation ordering leads to complete loss of the chiral organization and unique photonic properties and results in clear films with highly porous amorphous morphology. We suggest that at critical Debye charge screening length of below 3nm, the final nanocrystal organization is completely random as primary caused by long-range repulsive interactions outside of the intimate contact areas of high aspect ratio nanocrystals.

In conclusion, we suggest that final chiral organization critically depends upon balance repulsive long-range interparticle interactions as reflected by Debye charge screening length and surface charge density and attractive short-range interactions such as hydrophobic-hydrophobic and hydrogen bonding, playing in opposite directions. Considering that the effective charge and counter ions absorbance alter the electrostatic double layer of the nanocrystal surface are reflected in the Debye charge screening length, we suggest that final chiral optical properties of the films can be predicted by assessing nanocrystals Debye charge screening length in the suspension.

Finally, this research is based upon unique comprehensive and quantitative characterization of the molecular orientational order of cellulose nanocrystals in terms of their azimuthal distribution function and 2D orientation order parameter as combined with corresponding evaluation of other quantitative macroscopic ordering characteristics such as pitch length, twisting power, and twisting angle, rarely evaluated or even considered for CNC films. This analysis was conducted for CNC films obtained at identical processing (drying) conditions with the only variable condition being electrolyte concentration in initial CNC suspension. This research offers insights on tuning the orientation organization of CNC based composites by suggesting that the Debye charge screening length is a universal parameter that can predict the assembly trends and can be extended to other polysaccharides nanocrystals assemblies, such as chitin, due to their close chemical nature and interparticle interaction balance as should be further studied in future research.

SUPPORTING INFORMATION

Contains details on DLVO and surface charge density calculations and additional experimental results. This material is available free of charge online at [].

The authors declare no competing financial interest.

AKNOWLEDGEMENTS

Financial support for this research is provided by the NSF-CBET grant 180349, Air Force Research Laboratory grant FA8650-D-16-5404, and Air Force Office for Scientific Research grant FA9550-20-1-0305. The authors extend their gratitude to Dr. Julie Champion and Sydney Wimberley for providing help with zeta-potential measurements. We thank Dr. Saewon Kang for useful suggestions and critical comments regarding CNC order parameter quantifications, and Dr. Nicholas Kotov for valuable discussion.

TOC Graphic

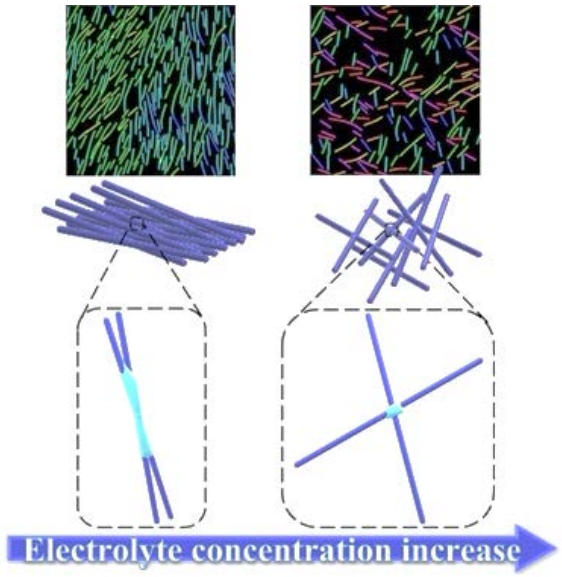

Schematic of the change in nanocrystals orientational organization with increase of electrolyte's concentration and corresponding orientational-colore-coded AFM images.

REFERENCES

[1] Wang, Z.; Cheng, F.; Winsor, T.; Liu, Y. Optical Chiral Metamaterials: A Review of the Fundamentals, Fabrication Methods and Applications. *Nanotechnology* **2016**, *27* (41), 412001.

[2] Yoo, S. J.; Park, Q.-H. Metamaterials and Chiral Sensing: A Review of Fundamentals and Applications. *Nanophotonics* **2019**, *8* (2), 249–261.

[3] Brolo, A. G. Plasmonics for Future Biosensors. *Nat. Photonics* **2012**, *6* (11), 709–713.

[4] Lv, P.; Lu, X.; Wang, L.; Feng, W. Nanocellulose-Based Functional Materials: From Chiral Photonics to Soft Actuator and Energy Storage. *Adv. Funct. Mater.* **2021**, 2104991.

[5] Xiong, R.; Grant, A. M.; Ma, R.; Zhang, S.; Tsukruk, V. V. Naturally-Derived Biopolymer Nanocomposites: Interfacial Design, Properties and Emerging Applications. *Mater. Sci. Eng. R Rep.* **2018**, *125*, 1–41.

[6] Kim, M.; Lee, H.; Krecker, M. C.; Bukharina, D.; Nepal, D.; Bunning, T. J.; Tsukruk, V. V. Switchable Photonic Bio-Adhesive Materials. *Adv. Mater.* **2021**, *33* (42), 2103674.

[7] Schütz, C.; Salajkova, M.; Noh, J. H.; Hyun Park, J.; Scalia, G.; Bergström, L. Cellulose Nanocrystal-Based Materials: From Liquid Crystal Self-Assembly and Glass Formation to Multifunctional Thin Films. *NPG Asia Mater.* **2014**, *6*, e80.

[8] Kontturi, E.; Laaksonen, P.; Linder, M. B.; Nonappa; Gröschel, A. H.; Rojas, O. J.; Ikkala, O. Advanced Materials Through Assembly of Nanocelluloses. *Adv. Mater.* **2018**, *30* (24), 1703779.

[9] Johansson, C.; Bras, J.; Mondragon, I.; Nechita, P.; Plackett, D.; Šimon, P.; Gregor Svetec, D.; Virtanen, S.; Giacinti Baschetti, M.; Breen, C.; Aucejo, S. Renewable Fibers and Bio-Based Materials for Packaging Applications – a Review of Recent Developments. *BioResources* **2012**, *7* (2), 2506–2552.

[10] Kim, T.; Tran, T. H.; Hwang, S. Y.; Park, J.; Oh, D. X.; Kim, B.-S. Crab-on-a-Tree: All Biorenewable, Optical and Radio Frequency Transparent Barrier Nanocoating for Food Packaging. *ACS Nano* **2019**, *13* (4), 3796–3805.

[11] Kim, M.; Lee, H.; Snipes, R. T.; Han, M. J.; Tsukruk, V. V. CO-Assembly of Biosynthetic Chiral Nematic Adhesive Materials with Dynamic Polarized Luminescence. *Small* **2021**, *18* (2), 2104340.

[12] Moon, R. J.; Martini, A.; Nairn, J.; Simonsen, J.; Youngblood, J. Cheminform Abstract: Cellulose Nanomaterials Review: Structure, Properties and Nanocomposites. *ChemInform* **2011**, *42* (42), 3941-3994.

[13] Beck-Candanedo, S.; Roman, M.; Gray, D. G. Effect of Reaction Conditions on the Properties and Behavior of Wood Cellulose Nanocrystal Suspensions. *Biomacromolecules* **2005**, *6* (2), 1048–1054.

[14] Parker, R. M.; Guidetti, G.; Williams, C. A.; Zhao, T.; Narkevicius, A.; Vignolini, S.; Frka-Petesic, B. The Self-Assembly of Cellulose Nanocrystals: Hierarchical Design of Visual Appearance. *Adv. Mater.* **2017**, *30* (19), 1704477.

[15] Onsager, L. The Effects of Shape on the Interaction of Colloidal Particles. *Ann. N. Y. Acad.* **1949**, *51* (4), 627–659.

[16] Stroobants, A.; Lekkerkerker, H. N.; Odijk, T. Effect of Electrostatic Interaction on the Liquid Crystal Phase Transition in Solutions of Rodlike Polyelectrolytes. *Macromolecules* **1986**, *19* (8), 2232–2238.

[17] Hanley, S. J., Revol, J.-F., Godbout, L. & Gray, D. G. Atomic force microscopy and transmission electron microscopy of cellulose from Micrasterias denticulata; evidence for a chiral helical microfibril twist. *Cellulose* **1997**, *4* (3), 209-220.

[18] Wang, P.-X.; Hamad, W. Y.; MacLachlan, M. J. Structure and Transformation of Tactoids in Cellulose Nanocrystal Suspensions. *Nat. Commun.* **2016**, *7*, article number: 11515.

[19] Parsegian, V.A. *Van der Waals Forces: A Handbook for Biologists, Chemists, Engineers, and Physicists.* Cambridge University Press: New York, **2006**.

[20] Stroobants, A., Lekkerkerker, H. N. W. & Odijk, T. Effect of electrostatic interaction on the liquid crystal phase transition in solutions of rodlike polyelectrolytes. *Macromolecules* **1986**, *19*, 2232–2238.

[21] Usov, I.; Nyström, G.; Adamcik, J.; Handschin, S.; Schütz, C.; Fall, A.; Bergström, L.; Mezzenga, R. Understanding Nanocellulose Chirality and Structure–Properties Relationship at the Single Fibril Level. *Nat. Commun.* **2015**, *6*, article number:7564.

[22] Ogawa, Y. Electron Microdiffraction Reveals the Nanoscale Twist Geometry of Cellulose Nanocrystals. *Nanoscale* **2019**, *11* (45), 21767–21774.

[23] Paavilainen, S.; Róg, T.; Vattulainen, I. Analysis of Twisting of Cellulose Nanofibrils in Atomistic Molecular Dynamics Simulations. *J. Phys. Chem. B* **2011**, *115* (14), 3747–3755.

[24] Hadden, J. A.; French, A. D.; Woods, R. J. Unraveling Cellulose Microfibrils: A Twisted Tale. *Biopolymers* **2013**, *99* (10), 746–756.

[25] Nakata, M. Zanchetta, G. Chapman, B.D. Jones, C.D. Cross, J.O. Pindak, R. Bellini, T. Clark, N.A. End-to-end stacking and liquid crystal condensation of 6-to-20-base pair DNA duplexes, *Science* **2007**, *318*, 1276.

[26] Strzelecka, T.E.; Davidson, M.W.; Rill, R.L. Multiple liquid crystal phases of DNA at high concentrations. *Nature* **1988**, *331*, 457–460.

[27] Dogic, Z.; Fraden, S. Cholesteric Phase in Virus Suspensions. *Langmuir* **2000**, *16*, 7820–7824

[28] Dogic, Z.; Fraden, S. Ordered phases of filamentous viruses. *Curr. Opin. Colloid Interface Sci.* **2006**, *11*, 47–55

[29] Kornyshev, A. A.; Leikin, S. Theory of Interaction between Helical Molecules. *J. Chem. Phys.* **1997**, *107* (9), 3656–3674.

[30] Strzelecka, T. E., Davidson, M. W. & Rill, R. L. Multiple liquid crystal phases of DNA at high concentrations. *Nature* **1988**, *331,* 457–460.

[31] Kornyshev, A. A.; Leikin, S. Twist in Chiral Interaction between Biological Helices. *Phys. Rev. Lett.* **2000**, *84* (11), 2537–2540.

[32] Schütz, C.; Agthe, M.; Fall, A. B.; Gordeyeva, K.; Guccini, V.; Salajková, M.; Plivelic, T. S.; Lagerwall, J. P. F.; Salazar-Alvarez, G.; Bergström, L. Rod Packing in Chiral Nematic Cellulose Nanocrystal Dispersions Studied by Small-Angle X-Ray Scattering and Laser Diffraction. *Langmuir* **2015**, 31 (23), 6507–6513.

[33] Reid, M. S.; Kedzior, S. A.; Villalobos, M.; Cranston, E. D. Effect of Ionic Strength and Surface Charge Density on the Kinetics of Cellulose Nanocrystal Thin Film Swelling. *Langmuir* **2017**, *33* (30), 7403–7411.

[34] Pan, J.; Hamad, W.; Straus, S. K. Parameters Affecting the Chiral Nematic Phase of Nanocrystalline Cellulose Films. *Macromolecules* **2010**, *43* (8), 3851–3858.

[35] Mu, X.; Gray, D. G. Formation of Chiral Nematic Films from Cellulose Nanocrystal Suspensions Is a Two-Stage Process. *Langmuir* **2014**, *30* (31), 9256–9260.

[36] Dong, X. M.; Gray, D. G. Effect of Counterions on Ordered Phase Formation in Suspensions of Charged Rodlike Cellulose Crystallites. *Langmuir* **1997**, *13* (8), 2404–2409.

[37] Pan, J.; Hamad, W.; Straus, S. K. Parameters Affecting the Chiral Nematic Phase of Nanocrystalline Cellulose Films. *Macromolecules* **2010**, *43* (8), 3851–3858.

[38] Dumanli, A. G.; Kamita, G.; Landman, J.; van der Kooij, H.; Glover, B. J.; Baumberg, J. J.; Steiner, U.; Vignolini, S. Controlled, Bio-Inspired Self-Assembly of Cellulose-Based Chiral Reflectors. *Adv. Opt. Mater.* **2014**, *2* (7), 646–650.

[39] De France, K. J.; Yager, K. G.; Hoare, T.; Cranston, E. D. Cooperative Ordering and Kinetics of Cellulose Nanocrystal Alignment in a Magnetic Field. *Langmuir* **2016**, *32* (30), 7564–7571.

[40] Li, C.; Evans, J.; Wang, N.; Guo, T.; He, S. Ph Dependence of the Chirality of Nematic Cellulose Nanocrystals. *Sci. Rep.* **2019**, *9* (1), 11290.

[41] Bruckner, J. R.; Kuhnhold, A.; Honorato-Rios, C.; Schilling, T.; Lagerwall, J. P. Enhancing Self-Assembly in Cellulose Nanocrystal Suspensions Using High-Permittivity Solvents. *Langmuir* **2016**, *32* (38), 9854–9862.

[42] Orts, W. J.; Godbout, L.; Marchessault, R. H.; Revol, J.-F. Enhanced Ordering of Liquid Crystalline Suspensions of Cellulose Microfibrils: a Small Angle Neutron Scattering Study. *Macromolecules* **1998**, *31* (17), 5717–5725.

[43] Araki, J.; Kuga, S. Effect of Trace Electrolyte on Liquid Crystal Type of Cellulose Microcrystals. *Langmuir* **2001**, *17* (15), 4493–4496.

[44] Abitbol, T.; Kam, D.; Levi-Kalisman, Y.; Gray, D. G.; Shoseyov, O. Surface Charge Influence on the Phase Separation and Viscosity of Cellulose Nanocrystals. *Langmuir* **2018**, *34* (13), 3925–3933.

[45] Dong, X. M.; Gray, D. G. Effect of Counterions on Ordered Phase Formation in Suspensions of Charged Rodlike Cellulose Crystallites. *Langmuir* **1997**, *13* (8), 2404–2409.

[46] Dong, X. M.; Kimura, T.; Revol, J.-F.; Gray, D. G. Effects of Ionic Strength on the Isotropic−Chiral Nematic Phase Transition of Suspensions of Cellulose Crystallites. *Langmuir* **1996**, *12* (8), 2076–2082.

[47] Cherhal, F.; Cousin, F.; Capron, I. Influence of Charge Density and Ionic Strength on the Aggregation Process of Cellulose Nanocrystals in Aqueous Suspension, as Revealed by Small-Angle Neutron Scattering. *Langmuir* **2015**, *31* (20), 5596–5602.

[48] Beck-Candanedo, S.; Roman, M.; Gray, D. G. Effect of Reaction Conditions on the Properties and Behavior of Wood Cellulose Nanocrystal Suspensions. *Biomacromolecules* **2005**, *6* (2), 1048–1054.

[49] Reid, M. S.; Kedzior, S. A.; Villalobos, M.; Cranston, E. D. Effect of Ionic Strength and Surface Charge Density on the Kinetics of Cellulose Nanocrystal Thin Film Swelling. *Langmuir* **2017**, *33* (30), 7403–7411.

[50] Cao, T.; Elimelech, M. Colloidal Stability of Cellulose Nanocrystals in Aqueous Solutions Containing Monovalent, Divalent, and Trivalent Inorganic Salts. *J. Colloid Interface Sci.* **2021**, *584*, 456–463.

[51] Qu, D.; Zheng, H.; Jiang, H.; Xu, Y.; Tang, Z. Chiral Photonic Cellulose Films Enabling Mechano/Chemo Responsive Selective Reflection of Circularly Polarized Light. *Adv. Opt. Mater.* **2019**, *7*, 1801395

[52] Shen, Z.; Wang, T.; Shi, L.; Tang, Z.; Liu, M. Strong circularly polarized luminescence from the supramolecular gels of an achiral gelator: tunable intensity and handedness. *Chem. Sci.* **2015**, *6*, 4267-4272.
[53] Dolamic, I.; Knoppe, S.; Dass, A.; Bürgi, T. First enantioseparation and circular dichroism spectra of Au38 clusters protected by achiral ligands. *Nat. Commun.* **2012**, *3*, 798.
[54] McConney, M. E.; Singamaneni, S.; Tsukruk, V. V. Probing Soft Matter with the Atomic Force Microscopies: Imaging and Force Spectroscopy. *Poly. Rev.* **2010**, *50* (3), 235–286.
[55] Persson, N. E.; McBride, M. A.; Grover, M. A.; Reichmanis, E. Automated Analysis of Orientational Order in Images of Fibrillar Materials. *Chem. Mater.* **2016**, *29* (1), 3–14.
[56] Xiong, Y.; Liu, X.; Xiong, H. Aggregation Modeling of the Influence of Ph on the Aggregation of Variably Charged Nanoparticles. *Sci. Rep.* **2021**, *11* (1), 17386.
[57] Hyde, A. M.; Zultanski, S. L.; Waldman, J. H.; Zhong, Y.-L.; Shevlin, M.; Peng, F. General Principles and Strategies for Salting-out Informed by the Hofmeister Series. *Org Process Res Dev*. **2017**, *21* (9), 1355–1370.
[58] Beck-Candanedo, S.; Roman, M.; Gray, D. G. Effect of Reaction Conditions on the Properties and Behavior of Wood Cellulose Nanocrystal Suspensions. *Biomacromolecules* **2005**, *6* (2), 1048–1054.
[59] Abitbol, T.; Kam, D.; Levi-Kalisman, Y.; Gray, D. G.; Shoseyov, O. Surface Charge Influence on the Phase Separation and Viscosity of Cellulose Nanocrystals. *Langmuir* **2018**, *34* (13), 3925–3933.
[60] 4 Su, G.; Zhou, H.; Mu, Q.; Zhang, Y.; Li, L.; Jiao, P.; Jiang, G.; Yan, B. Effective Surface Charge Density Determines the Electrostatic Attraction between Nanoparticles and Cells. J. Phys. Chem. C 2012, 116 (8), 4993–4998
[61] Ge, Z.; Wang, Y. Estimation of Nanodiamond Surface Charge Density from Zeta Potential and Molecular Dynamics Simulations. *J. Phys. Chem. B* **2016**, *121* (15), 3394–3402.
[62] Israelachvili, J. N. *Intermolecular and Surface Forces.* Academic Press: 2011; p 313.
[63] Trefalt, G.; Behrens, S. H.; Borkovec, M. Charge Regulation in the Electrical Double Layer: Ion Adsorption and Surface Interactions. *Langmuir* **2015**, *32* (2), 380–400.
[64] Habibi, Y.; Lucia, L. A.; Rojas, O. J. Cellulose Nanocrystals: Chemistry, Self-Assembly, and Applications. *Chem. Rev.* **2010**, *110* (6), 3479–3500.
[65] Tatsumi, M.; Teramoto, Y.; Nishio, Y. Polymer Composites Reinforced by Locking-in a Liquid-Crystalline Assembly of Cellulose Nanocrystallites. *Biomacromolecules* **2012**, *13* (5), 1584–1591.
[66] Bouligand, Y.; Soyer, M.-O.; Puiseux-Dao, S. La structure fibrillaire et l'orientation des chromosomes chez les Dinoflagellés. *Chromosoma* **1968**, *24*, 251–287.
[67] Vignolini, S.; Rudall, P. J.; Rowland, A. V.; Reed, A.; Moyroud, E.; Faden, R. B.; Baumberg, J. J.; Glover, B. J.; Steiner, U. Pointillist Structural Color in Pollia Fruit. *Proc. Natl. Acad. Sci.* **2012**, *109* (39), 15712–15715.
[68] Kleman, M. Defects in Liquid Crystals. *Rep. Prog. Phys.* **1989**, *52* (5), 555–654.
[69] Wang, P.-X.; Hamad, W. Y.; MacLachlan, M. J. Structure and Transformation of Tactoids in Cellulose Nanocrystal Suspensions. *Nat. Commun.* **2016**, *7* (1), 11515.
[70] Diaz, J. A.; Wu, X.; Martini, A.; Youngblood, J. P.; Moon, R. J. Thermal Expansion of Self-Organized and Shear-Oriented Cellulose Nanocrystal Films. *Biomacromolecules* **2013**, *14* (8), 2900–2908.
[71] Guccini, V.; Kumar, S.; Trushkina, Y.; Nagy, G.; Schütz, C.; Salazar-Alvarez, G. Tuning the Magnetic Alignment of Cellulose Nanocrystals from Perpendicular to Parallel Using Lepidocrocite Nanoparticles. *Chemrxiv* **2019**, https://doi.org/10.26434/chemrxiv.8061839 (accessed 2022-04-22)
[72] Chowdhury, R. A.; Peng, S. X.; Youngblood, J. Improved Order Parameter (Alignment) Determination in Cellulose Nanocrystal (CNC) Films by a Simple Optical Birefringence Method. *Cellulose* **2017**, *24* (5), 1957–1970.
[73] Zhang, X.; Kang, S.; Adstedt, K.; Xiong, R.; Yu, J.; Tsukruk, V. V. Magnetic Nanoparticle-Decorated Bacterial Nanocelluloses for Uniaxial Liquid Crystal Phases and Fast Actuating Materials. *Nat. Comm.*, *in print* **2022**.
[74] Mohanty, S. Liquid Crystals — the 'Fourth' Phase of Matter. *Resonance* **2003**, *8* (11), 52–70.
[75] Chowdhury, R. A.; Nuruddin, M.; Clarkson, C.; Montes, F.; Howarter, J.; Youngblood, J. P. Cellulose Nanocrystal (CNC) Coatings with Controlled Anisotropy as High-Performance Gas Barrier Films. *ACS Appl. Mater. Interfaces* **2018**, *11* (1), 1376–1383.
[76] Frka-Petesic, B.; Sugiyama, J.; Kimura, S.; Chanzy, H.; Maret, G. Negative Diamagnetic Anisotropy and Birefringence of Cellulose Nanocrystals. *Macromolecules* **2015**, *48* (24), 8844–8857.
[77] Sanchez-Botero, L.; Dimov, A. V.; Li, R.; Smilgies, D.-M.; Hinestroza, J. P. In Situ and Real-Time Studies, via Synchrotron X-Ray Scattering, of the Orientational Order of Cellulose Nanocrystals during Solution Shearing. *Langmuir* **2018**, *34* (18), 5263–5272.

[78] Chowdhury, R. A.; Peng, S. X.; Youngblood, J. Improved Order Parameter (Alignment) Determination in Cellulose Nanocrystal (CNC) Films by a Simple Optical Birefringence Method. *Cellulose* **2017**, *24* (5), 1957–1970.
[79] Brown, G. H.; Dome, J. W.; Neff, V. D. Structure and Physical Properties of Liquid Crystals. *Crit. Rev. Solid State Mater. Sci.* **1970**, *1* (3), 303–379.
[80] Nuruddin, M.; Chowdhury, R. A.; Lopez-Perez, N.; Montes, F. J.; Youngblood, J. P.; Howarter, J. A. Influence of Free Volume Determined by Positron Annihilation Lifetime Spectroscopy (Pals) on Gas Permeability of Cellulose Nanocrystal Films. *ACS Appl. Mater. Interfaces* **2020**, *12* (21), 24380–24389.
[81] Zhang, Y. P.; Chodavarapu, V. P.; Kirk, A. G.; Andrews, M. P. Structured Color Humidity Indicator from Reversible Pitch Tuning in Self-Assembled Nanocrystalline Cellulose Films. *Sens. Actuators B: Chem.* **2013**, *176*, 692–697.
[82] Schütz, C.; Agthe, M.; Fall, A. B.; Gordeyeva, K.; Guccini, V.; Salajková, M.; Plivelic, T. S.; Lagerwall, J. P.; Salazar-Alvarez, G.; Bergström, L. Rod Packing in Chiral Nematic Cellulose Nanocrystal Dispersions Studied by Small-Angle X-Ray Scattering and Laser Diffraction. *Langmuir* **2015**, *31* (23), 6507–6513.
[83] Ma, W.; Xu, L.; de Moura, A. F.; Wu, X.; Kuang, H.; Xu, C.; Kotov, N. A. Chiral Inorganic Nanostructures. *Chem. Rev.* **2017**, *117* (12), 8041–8093.
[84] M. R. Wilson, D. J. Earl, Calculating the helical twisting power of chiral dopants. *J. Mater. Chem.* **2001**, *11*, 2672.
[85] Wang, B.; Walther, A. Self-Assembled, Iridescent, Crustacean-Mimetic Nanocomposites with Tailored Periodicity and Layered Cuticular Structure. *ACS Nano* **2015**, *9* (11), 10637–10646.
[86] Yang, S.; Zhang, Y.; Zhang, X.; Xu, J. The Influence of Ph on a Hydrogen-Bonded Assembly Film. *Soft Matter* **2007**, *3* (4), 463–469.
[87] Adstedt, K.; Popenov, E. A.; Pierce, K. J.; Xiong, R.; Geryak, R.; Cherpak, V.; Nepal, D.; Bunning, T. J.; Tsukruk, V. V. Chiral Cellulose Nanocrystals with Intercalated Amorphous Polysaccharides for Controlled Iridescence and Enhanced Mechanics. *Adv. Funct. Mater.* **2020**, *30* (49), 2003597.
[88] Korolovych, V. F.; Cherpak, V.; Nepal, D.; Ng, A.; Shaikh, N. R.; Grant, A.; Xiong, R.; Bunning, T. J.; Tsukruk, V. V. Cellulose Nanocrystals with Different Morphologies and Chiral Properties. *Polymer* **2018**, *145*, 334–347.
[89] Govorov, A. O. Fan, Z. Theory of chiral plasmonic nanostructures comprising metal nanocrystals and chiral molecular media. *Chem. Phys. Chem.* **2012**, *13*, 2551–2560.
[90] Gregory, J. Interaction of unequal double layers at constant charge. *J. Colloid Interface Sci* **1975**, *51*, 44-51.